

Lamination of organic solar cells and organic light emitting devices: Models and experiments

O. K. Oyewole, D. Yu, J. Du, J. Asare, V. C. Anye, A. Fashina, M. G. Zebaze Kana, and W. O. Soboyejo

Citation: [Journal of Applied Physics](#) **118**, 075302 (2015); doi: 10.1063/1.4928729

View online: <http://dx.doi.org/10.1063/1.4928729>

View Table of Contents: <http://scitation.aip.org/content/aip/journal/jap/118/7?ver=pdfcov>

Published by the [AIP Publishing](#)

Articles you may be interested in

[Adhesion in flexible organic and hybrid organic/inorganic light emitting device and solar cells](#)

[J. Appl. Phys.](#) **116**, 074506 (2014); 10.1063/1.4892393

[Semitransparent organic solar cells with hybrid monolayer graphene/metal grid as top electrodes](#)

[Appl. Phys. Lett.](#) **102**, 113303 (2013); 10.1063/1.4798254

[Lambertian white top-emitting organic light emitting device with carbon nanotube cathode](#)

[J. Appl. Phys.](#) **112**, 114505 (2012); 10.1063/1.4767439

[Two examples of organic opto-electronic devices: Light emitting diodes and solar cells](#)

[Am. J. Phys.](#) **76**, 1130 (2008); 10.1119/1.2976333

[Organic light-emitting devices integrated with solar cells: High contrast and energy recycling](#)

[Appl. Phys. Lett.](#) **90**, 173507 (2007); 10.1063/1.2732181

An advertisement for the journal AIP APL Photonics. The background is a vibrant orange and red gradient with a sunburst effect. On the left, there is a small image of the journal cover, which features a blue and white abstract design. A yellow starburst graphic with the words 'OPEN ACCESS' is overlaid on the cover. To the right of the cover, the text 'Launching in 2016!' is written in a large, white, sans-serif font. Below this, the text 'The future of applied photonics research is here' is written in a smaller, white, sans-serif font. In the bottom right corner, the AIP APL Photonics logo is displayed, consisting of the letters 'AIP' in a large, white, sans-serif font, followed by a vertical line and the words 'APL Photonics' in a smaller, white, sans-serif font.

Lamination of organic solar cells and organic light emitting devices: Models and experiments

O. K. Oyewole,^{1,2} D. Yu,^{3,4} J. Du,^{3,4,5} J. Asare,¹ V. C. Anye,⁶ A. Fashina,¹
 M. G. Zebaze Kana,² and W. O. Soboyejo^{3,4,6,a)}

¹*Department of Theoretical and Applied Physics, African University of Science and Technology, Km 10 Airport Road, Galadimawa, Abuja, Federal Capital Territory, Nigeria*

²*Department of Materials Science and Engineering, Kwara State University, P.M.B 1530, Ilorin, Kwara State, Nigeria*

³*Department of Mechanical and Aerospace Engineering, Princeton University, Olden Street, Princeton, New Jersey 08544, USA*

⁴*Princeton Institute of Science and Technology of Materials, Princeton University, 70 Prospect Street, Princeton, New Jersey 08544, USA*

⁵*Department of Mechanical and Nuclear Engineering, The Pennsylvania State University, 137 Reber Building, University Park, Pennsylvania, USA*

⁶*Department of Materials Science and Engineering, African University of Science and Technology, Km 10 Airport Road, Galadimawa, Abuja, Federal Capital Territory, Nigeria*

(Received 20 May 2015; accepted 5 August 2015; published online 18 August 2015)

In this paper, a combined experimental, computational, and analytical approach is used to provide new insights into the lamination of organic solar cells and light emitting devices at macro- and micro-scales. First, the effects of applied lamination force (on contact between the laminated layers) are studied. The crack driving forces associated with the interfacial cracks (at the bi-material interfaces) are estimated along with the critical interfacial crack driving forces associated with the separation of thin films, after layer transfer. The conditions for successful lamination are predicted using a combination of experiments and computational models. Guidelines are developed for the lamination of low-cost organic electronic structures. © 2015 AIP Publishing LLC.

[<http://dx.doi.org/10.1063/1.4928729>]

I. INTRODUCTION

In the recent years, several deposition techniques have been used for the fabrication of organic solar cells and organic light emitting devices (OLEDs).^{1–5} These include cold welding,⁶ transfer printing,⁷ and lamination^{1–4} techniques. In the case of lamination, deposition parameters, such as applied force for pre-lamination, pull-off force, and surface roughness must be controlled for successful lamination.^{7,8} In most cases, the presence of particles (e.g., silicon, dust, and organic materials) in clean room environment cannot be ignored. Such particles are trapped at the interfaces between layers during the fabrication of OLEDs and organic solar cells (organic photovoltaic cells (OPVs)).⁸ This results in the fabrication of micro-voids and partial contacts at the interfaces of layered electronics.^{6,8}

Furthermore, during lift-off (separation of stamp from the transferred layer) in the process of lamination, stress concentrations occur at the edges of the entrapped voids/cracks. Since these can lead to interfacial plasticity or cracking, there is a need to understand the stresses and crack driving forces associated with contacts and pull-off stages of pre-lamination and pull-off forces. It is also important to identify

the processing windows for contact and pull-off without indicating damage to organic electronic devices.

Since OPVs and OLEDs require charge transport across interfaces in layered structure (as shown in Figure 1), the process of charge transport across interfaces can be hindered by entrapped voids/cracks that are formed during contact and lamination processes.⁹ Conversely, the contact between adjacent layers can be enhanced by increased pressure and interfacial adhesion. This can improve charge transport across layer structures that are relevant to organic solar cells and light emitting devices. However, excessive pressure can also lead to sink in of the interfacial impurities and damage to the devices.¹⁰ There is, therefore, a need for models that can guide the design of impurities.

Prior work^{1,3,9} has been carried out on the lamination of solar cells, light emitting devices, and flexible batteries. Lee *et al.*¹ have demonstrated the lamination of top electrode in semitransparent organic photovoltaic cells. Low temperature lamination processes have also been studied by Guo *et al.*,³ while Huang *et al.*² have described a one-step process for the fabrication of semitransparent polymer solar cells. Furthermore, Hu *et al.*¹¹ have used a lamination process to integrate Li-ion battery materials onto a single sheet of paper. Cao *et al.*,⁸ Kim *et al.*,¹² and Akande *et al.*⁶ have reported a cold welding technique for the fabrication of gold-gold and gold-silver thin films that are relevant to OLEDs, while a computational approach has been used by Tucker *et al.*⁷ to improve the overall quality of film transferred during the lamination of electronic devices.

^{a)} Author to whom correspondence should be addressed. Electronic mail: soboyejo@princeton.edu. Phone: +1-609-258-5609, Fax: +1-609-258-5877. Present address: Department of Mechanical and Aerospace Engineering, Engineering Quadrangle, Room D404B, Princeton, New Jersey 08544, USA.

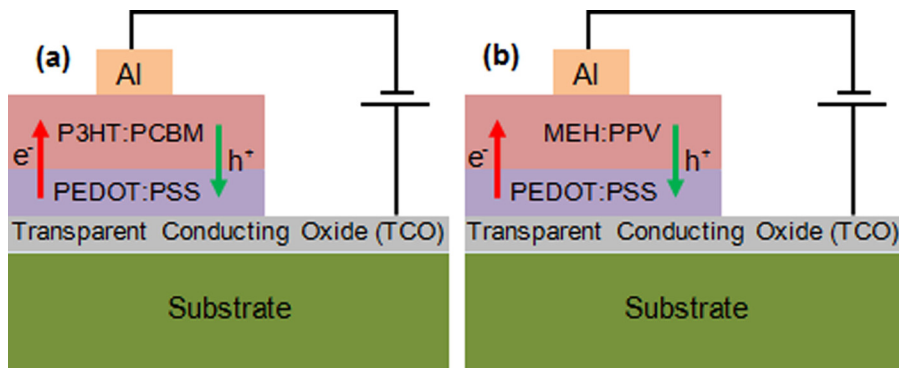


FIG. 1. Schematics of simple (a) OPV structure and (b) OLED structure.

However, most of the prior work on the lamination of organic solar cells and organic light emitting devices has involved experimental work, with limited modeling. There is, therefore, a need for combined experimental, computational, and analytical approaches that are designed to provide general insights for the design of lamination processes that are relevant to OPVs and OLEDs. This will be explored in this paper using a combination of experiments and models that are designed to provide insights for the design of lamination processes that are relevant to OLEDs and OPVs. Following the introduction in Section I, contact and pull-off models are presented in Section II. The experimental procedures are then described in Section III, before presenting the results and discussion in Section IV. Salient conclusions arising from this work are summarized in Section V.

II. MODELING

In an effort to laminate low-cost organic solar cells, analytical modeling and computational modeling were used to study interfacial contacts that occur during pre-lamination, as well as the interfacial failure that occurs during the interfacial separation associated with the lamination process. The success of the lamination depends on which of the two interfaces involved in the process fails first (Figure 2).⁷

If the top interface (between the poly-di-methyl-siloxane (PDMS) stamp and the transferred layer) fails before the critical condition for bottom interfacial failure is reached between the transferred layer and the substrate, the lamination is considered to be successful.⁷ However, if the interface between the transferred layer and the substrate fails before

the critical condition for interfacial failure between the PDMS stamp and the transferred layer, the lamination is deemed unsuccessful. The various possible results of separation in the lamination process have been described by Tucker *et al.*⁷

A. Adhesive surface contacts

Structures of OPV and OLED cells are typically fabricated from multilayers in contact. Each of these layers should have the right work function alignment for increased charge transport to occur across the interfaces. However, improved contact at inorganic/organic and organic/organic material interfaces can also be enhanced by improved adhesion¹³ and the application of pressure.¹⁰ There is, therefore, a need to explore the effects of adhesion and pressure on the contacts between adjacent layers in organic electronic structures.

In the case of low cost lamination techniques that are used for the fabrication of OPVs and OLEDs, the layer to be laminated is often coated onto a PDMS stamp before transferring it to a substrate. During this process, as the coated-PDMS stamp approaches the layered substrate (Figure 3(a)), the presence of distributed particles limits the contact with the underlying substrate. This results in the formation of voids as the layers wrap around the surface of impurities to create interfacial voids.⁸ Such particles have been revealed in prior focused ion beam microscopy work by Akande.⁶ These have shown that nano-scale and micro-scale voids can form at the interfaces, depending on the sizes of the interfacial impurities (Figures 3(c) and 3(d)). Hence, the

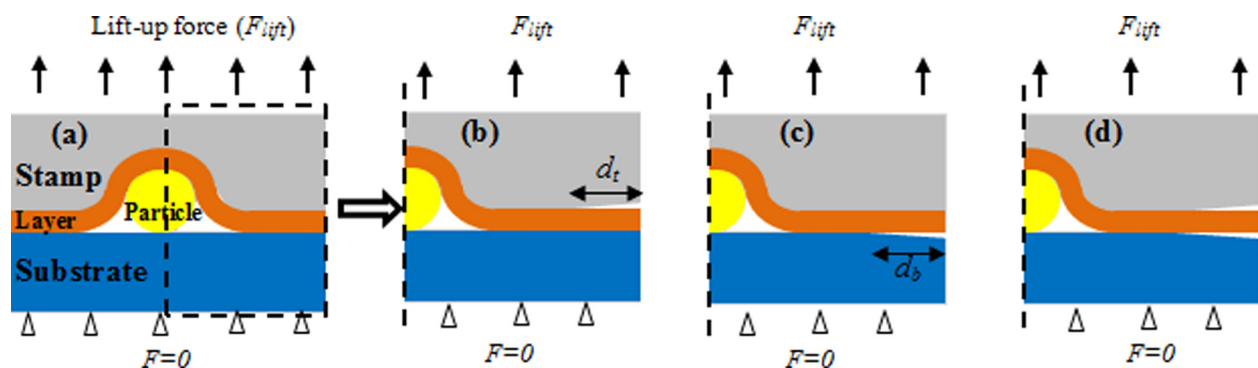


FIG. 2. Schematics of micro scale models of interfacial fracture during the lift-off process (a) model of the lift-off process after the press down of the layer on the substrate, (b) axisymmetric model of successful lift-off, (c) axisymmetric model of unsuccessful lift-off, and (d) axisymmetric model of partial interfacial fracture.

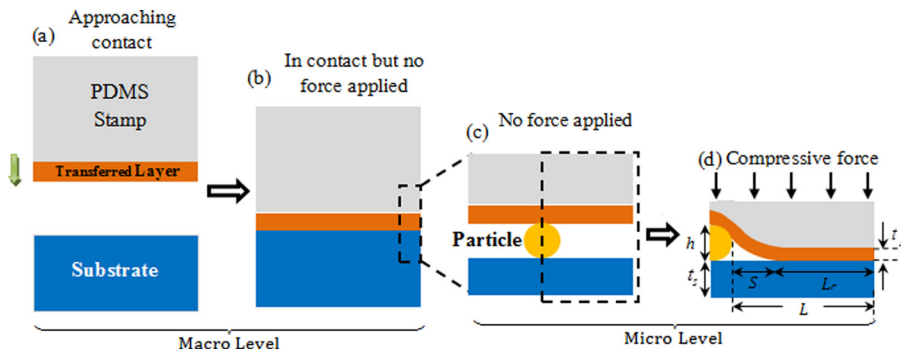


FIG. 3. Schematics of micro/macro scale models of adhesion and contact during pre-lamination process of the lamination.

application of pressure can increase the contact of stamps around interfaces that are relevant to OPVs and OLEDs.

The surface contact length that can be achieved can be estimated using an analytical model of contact around a dust particle. This is done by considering a scenario in which the particles of heights, h , are idealized between the transferred layer of thickness, t_f , and the substrate of thickness, t_s . The transferred layer can be likened to a cantilever beam that bent to an S-shape (Fig. 2(d))^{6,8} under uniform compressed force, F , on the stamp. The length, L , of the layered structure is given by

$$L = S + L_c, \quad (1)$$

where L_c is the length of the contact and S is the length of the void. The relationship between the contact length and applied force, F , (the detailed derivation is presented in Appendix A) is given by

$$\frac{L_c}{L} = 1 - \left(\frac{3E_f t_f^3 h w}{2FL^3} \right)^{\frac{1}{4}}, \quad (2)$$

where w and E_f are the width and the Young's modulus of the transferred layer, respectively.

Using the material properties presented in Table I,^{7,10,14–17} the normalized contact length can be calculated as a function of the applied compressive force.

B. Fracture mechanics modeling

The lamination of a thin film layer from a coated stamp to a substrate is basically in two stages: pre-lamination and lift-off. During pre-lamination, a compressive force is applied to the stamp to ensure that the layer makes good contact with the substrate. In the case of lift-off, a lift-off force is applied to separate the stamp from the laminated layer. This lift-off process will be considered as an interfacial

fracture process in this study. During the pre-lamination process, the application of uniform compressive force (as described above in Sec. II A) can induce stresses in layered organic electronics. The stress concentrations become more significant when the dust particles are sandwiched between the interfaces. This can lead ultimately to interfacial crack growth and fracture in the layered structure.

Prior work on the fracture mechanics modeling of pre-lamination and interfacial fracture of OLEDs and OPVs has been carried out by Tucker *et al.*⁷ for transfer printing. However, the sizes of the particle can affect the interfacial mechanics during the separation of stamps from the laminated structures, as described by Cao *et al.*⁸ During the separation process at the micro scale (Figure 2), the following are possible:

- (i) steady interfacial delamination between the transferred layer and substrate—unsuccessful lamination (Figure 2(b));
- (ii) steady interfacial delamination between PDMS stamp and transferred layer—successful lamination (Figure 2(c));
- (iii) possible simultaneous delamination in interfaces of the transferred layer/substrate, and the PDMS stamp/transferred layer—partial lamination (Figure 2(d)).

In an effort to model the fracture processes involved in lift-off process, Figure 2 shows an idealized nano particle between the layered interfaces produced after pre-lamination. Edge cracks are also idealized between the transferred layer and stamp and/or between transferred layer and substrate. The energy release rates at the tips of the edge cracks are measures of the crack driving force. In general, the energy release rate of the interfacial crack between the laminated film and the substrate is a function of plane strain elastic moduli of the film, \bar{E}_f , and substrate, \bar{E}_s , the length of top interfacial crack, d_t , the length of the bottom interfacial crack, d_b , the thickness of the film, t_f , thickness of the substrate, t_s , and the lift-up stress, σ . This is given by

$$G = f(\bar{E}_s, \bar{E}_f, t_t, t_s, d_b, d_t, \sigma), \quad (3)$$

where $\bar{E}_f = E_f/(1 - \nu^2)$ and $\bar{E}_s = E_s/(1 - \nu^2)$. Using the Buckingham pi-theorem method of dimensional analysis (Appendix B), Equation (3) can be expressed as

$$G = f\left(\frac{\bar{E}_s}{\bar{E}_f}, \frac{t_s}{t_f}, \frac{d_b}{t_f}, \frac{d_t}{t_f}\right) \frac{\sigma^2 t_f}{\bar{E}_f}. \quad (4)$$

TABLE I. Properties of the materials used in the modeling.

Material	Young's modulus (GPa)	Poisson ratio	References
Particle	70	0.3	7
MEH:PPV	11.5	0.3	10
PEDOT:PSS	1.56	0.3	10
P3HT:PCBM	6.02	0.35	14
Glass	69	0.3	15
PDMS	0.003	0.3	16, 17

Since $\sigma = F_{\text{Lift-off}}/wL$, where $F_{\text{Lift-off}}$ is the lift-up force, Eq. (4) can be written as

$$G = f \left(\frac{\bar{E}_s}{\bar{E}_f}, \frac{t_s}{t_f}, \frac{d_b}{t_f}, \frac{d_t}{t_f} \right) \frac{F_{\text{Lift-off}}^2 t_f}{w^2 L^2 \bar{E}_f}, \quad (5)$$

where w and L are the width and length of the structure, respectively.

C. Computational modeling

The ABAQUS™ software package (ABAQUS 6.12, Dassault Systèmes Incorporation, Rhode Island) was used to simulate the changes of contact profiles between the transferred layer and the substrate during pre-lamination along with the possible interfacial failure during the separation of the stamp from the transferred (laminated) layer. First, the effects of applied forces (on the surface contact lengths of the active layers of OPV cells and OLEDs) were simulated on poly(3,4-ethylenedioxythiophene):polystyrene sulfonate (PEDOT:PSS)-coated substrates. It was also assumed that particles are sandwiched between the laminated layer and the substrate. The size ranges ($\sim 0.1 - 10 \mu\text{m}$) are typical of particles that are present in clean room environments. These include silicon, organics, and other dust particles that are often found in the clean room environment.⁸

By considering a unit width ($w = 1$), axisymmetric models were developed using the ABAQUS software package. A four-node elemental mesh was used. The elements were dense near the particles and the contact surface (Figure 4). The bottom boundary of the substrate was fixed for stability during the simulations, while a range of uniform forces (0 N-500 N) was applied to the top of the stamp (Figure 5). The materials used (Table I) were assumed to exhibit isotropic behavior. Also, the height of the particle was varied, while the length of the contact surface was

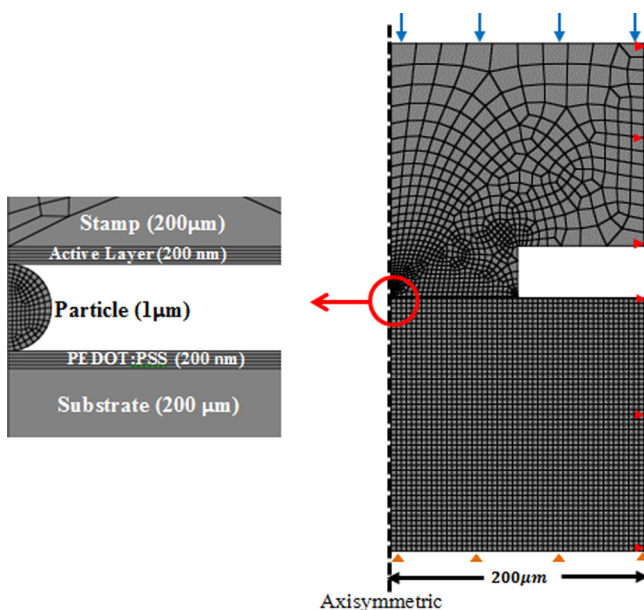


FIG. 4. Geometry and mesh of finite element model of surface contact during pre-lamination of active layers of organic solar cells and light emitting devices.

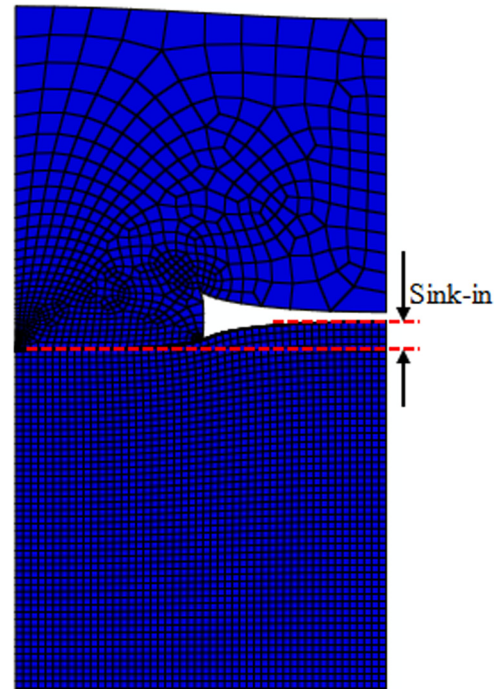


FIG. 5. FEM of surface contact model after applying a range of forces (0N-500N).

studied as a function of the applied force. This was done for laminating layers of model OPVs and OLEDs.

In the case of interfacial failure (during the separation of PDMS stamps from the laminated layered structures in the lift-off process in lamination), 2D models (with a unit width) were built using the ABAQUS software. These were used to study the interfacial cracking between the laminated layer and the stamp (top interface), as well as the interfacial cracking between the laminated layer and the substrate (bottom interface). Again, a four-node elemental mesh was used, while the elements were dense near the crack tips. The finite element simulations were used to determine the interfacial fracture energies corresponding to the lift-off forces that were applied to separate the stamps from the laminated film materials.

In the lamination process, two different interfaces (the top and the bottom) are possible. By assuming respective existing edge cracks of lengths, d_t and d_b , at the top and bottom interfaces, the energy release rate at the tip of the edge crack at the top interface is denoted as G_t , while the energy release rate at the tip of the edge crack at the bottom interface is denoted as G_b . The thicknesses of the layers were maintained constant, while the energy release rates of the crack tips were calculated using J-integral as functions of the crack length. The energy release rates of the interfacial crack tips were computed for a range of applied lift-off forces.

The success of the lamination process can be explained in form of differentials of the driving forces of the propagating cracks along the interfaces that are involved in the process.⁷ At a critical condition, the differential of the interfacial energy release rates (G_t^c and G_b^c) of the edge cracks at the top and bottom interfaces can be expressed as

$$\frac{G_t}{G_b} = \frac{G_t^c}{G_b^c}, \quad (6)$$

where G_t^c and G_b^c are the critical interfacial energy release rates at the top and bottom interfaces, respectively. If $G_t/G_b > G_t^c/G_b^c$, the interfacial crack will propagate along the top interface. This will result ultimately in the delamination of the stamp from the transferred layer. In this case, the lamination is successful. However, the lamination will be considered unsuccessful, if $G_t/G_b < G_t^c/G_b^c$; the crack propagates along the bottom interface, causing delamination of the laminated layer from the substrate. In these two scenarios, the lift-up force for successful lamination of materials in OPVs and OLEDs can be predicted.

III. EXPERIMENTAL METHODS

A. Pre-lamination of layers of OPV cells and OLEDs

First, the PDMS substrate was prepared by mixing a Sylgard 184 silicone elastomer curing agent with a Sylgard 184 silicone elastomer base (Dow Corning Corporation, Midland, MI) with a 1:10 weight ratio. Then, the mixture was then processed under a vacuum pressure of 6 kPa for 30 min. This was done to eliminate all of the possible bubbles. The processed PDMS was then poured into a flat aluminum mold with dimensions of 15 mm × 10 mm × 2 mm. This was followed by annealing in an oven at 80 °C for 2 h, resulting in the formation of an ~2 mm thick PDMS stamp. The PEDOT:PSS solution (Hareous, Clevios, Hanau, Germany) was spin-coated onto a clean glass slide at 3000 rpm for 1 min to obtain a film with thickness of 100 nm.

In the case of the OLED, the poly [2-methoxy-5-(2-ethyl-hexyloxy)-1,4-phenylene vinylene] (MEH-PPV) solute (Sigma Aldrich, St. Louis, MO) was mixed with chloroform (at a 5 g/l solute-solvent ratio) to form a solution. The mixture was stirred continuously for 6 h at room-temperature before passing it through a 0.45 μm teflon filter. The cured PDMS was attached to a flat stub using a double-sided tape. This was done before dip coating the PDMS stamp with MEH-PPV solution. The stub was then attached to the head of an Instron machine (Instron 5848, Canton, MA, USA) along with the PEDOT:PSS-coated glass plate that was fixed under the dip-coated PDMS stamp. The MEH-PPV was laminated onto PEDOT:PSS by applying loads in the ranges from 100 N to 500 N for 2 min before lift-off. The stamp was

lifted 3 mm apart from the laminated MEH-PPV with the head of the Instron testing machine moving up at a displacement rate of 0.01 mm/s.

For the lamination of the OPV cells, the poly (3-ethyl-thiophene) (P3HT) (Sigma Aldrich, St. Louis, MO):phenyl-C61-butyric acid methyl ester (PCBM) (Sigma Aldrich, St. Louis, MO) layer was first prepared by mixing P3HT and PCBM in chlorobenzene. This was mixed in ratio of 1:0.8 by weight. The mixture was then stirred continuously for 5 h at room temperature, before spin coating it onto the PDMS stamp at 750 rpm for 30 s. The P3HT:PCBM was laminated from the P3HT:PCBM-coated stamp to the PEDOT:PSS layer with the same protocol that was used for the lamination of the MEH-PPV layer in the OLED structure.

B. Pull-off of the laminated and spin-coated active layers

First, a sticky foam pad with a cross sectional area 25 mm × 8 mm was cut and attached to a stub using a double-sided tape. The stub was then attached to the head of an Instron testing machine, while the bottom of the substrate (P3HT:PCBM/PEDOT:PSS/glass) was attached to the bottom stub. Note that the double-sided tape covered the sectional area that was used to pull-off the laminated active layer. The sticky foam pad was then brought into contact with the P3HT:PCBM layer with a near zero force. This was done before scratching off the active layer on the border of the foam pad to maintain the same stress state in each sample. A schematic of the experimental set-up is presented in Figure 6.

A load of 100 N was applied to the pad for 60 s. This load was then maintained for another 60 s, before lifting up the head at a rate of 0.01 mm/s. The same protocol was applied for the pull-off of the laminated MEH-PPV, as well as the spin-coated MEH-PPV and P3HT:PCBM. In each case, the force-displacement curves were obtained. The surface of substrate (PEDOT:PSS/glass) was also observed using AFM.

IV. RESULTS AND DISCUSSION

A. Modeling of contact during pre-lamination

The effects of the compressive force (on the contacts between the active layers and PEDOT:PSS-coated substrates

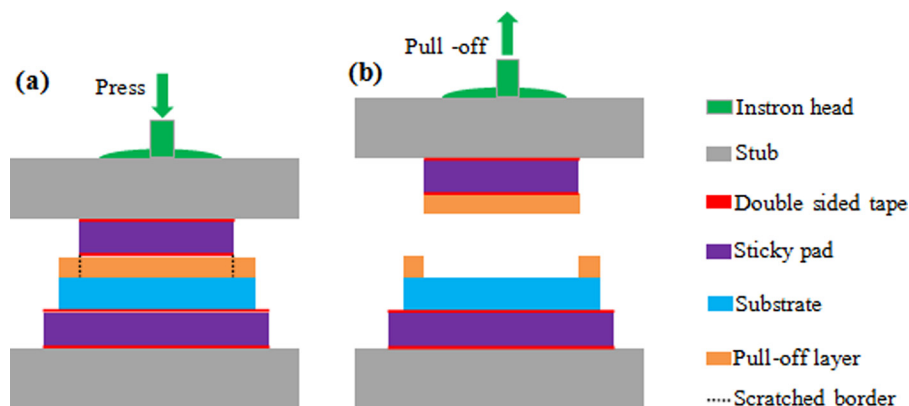


FIG. 6. Schematic of experimental pull-off of spin-coated and laminated layer, showing the (a) press down process and (b) pull-off process.

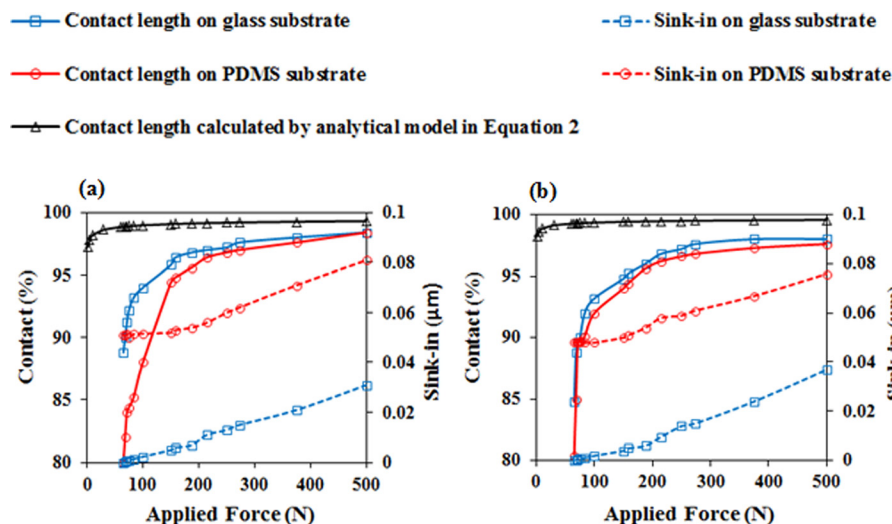


FIG. 7. Effects of force on contact profiles of (a) P3HT:PCBM on PEDOT:PSS-coated substrate and (b) MEH-PPV on PEDOT:PSS-coated substrate.

of the organic light emitting devices and organic solar cells) are presented in Figure 7. The results obtained from the analytical (Eq. (2)) and computational modeling show that the contact lengths between pre-lamination of P3HT:PCBM (Figure 7(a)) or MEH-PPV (Figure 7(b)) onto the substrates. These increase with increasing applied force.

The pre-laminated active layers sink more into the substrate as the applied force increases. The sink-in is also more significant in the case of flexible PDMS substrates. These results suggest that, in the case of rigid and flexible substrates, the desired interfacial contact between the active layers and substrates can be damaged due to excessive applied force. The results also show that, at an applied force of ~ 250 N, the predicted contact length is $\sim 95\%$ (by FEM) and $\sim 100\%$ (by analytical modeling).

B. Pre-lamination of active layers

In this section, the force needed to separate the stamp from the pre-laminated active layers is determined. It is important to note here that the stamp can be separated from pre-laminated layers if the interfacial contact between the active layers and the substrate is maintained with the applied pre-laminated compressive force. The force-displacement curves for successful pre-lamination of P3HT:PCBM and MEH-PPV onto PEDOT:PSS-coated glass are presented in Figure 8. First, the force increases with increasing displacement, before returning to zero force. At an applied compressive force of ~ 200 N, the force-displacement curves have a peak ~ 0.06 N for pre-lamination of P3HT:PCBM and

~ 1.10 N for pre-lamination of MEH-PPV. The peaks of the curves represent the interfacial work of adhesion in the top interfaces (stamp/P3HT:PCBM and stamp/MEH-PPV) of the active layers.

C. Pull-off experiments

The results of the pull-off tests (on the laminated and spin-coated active layers) are presented in Figure 9. The peaks of the force-displacement curves represent the interfacial adhesion force between the active layers and the PEDOT:PSS-coated substrates. In Figure 9, the adhesion force in laminated MEH:PPV/PEDOT:PSS (Figure 9(b)) is comparable to the adhesion force, when the P3HT:PCBM is spin-coated onto the substrate. In the case of P3HT:PCBM/PEDOT:PSS-coated glass, shown in Figures 9(c) and 9(d), the adhesion forces obtained from the lamination and spin-coating techniques are also comparable.

From the results, the adhesion forces at the interfaces of P3HT:PCBM/PEDOT:PSS-coated glass substrate and MEH:PPV/PEDOT:PSS-glass are more than the measured adhesion forces at the interfaces of Stamp/P3HT:PCBM (Figure 8(a)) and Stamp/MEH:PPV (Figure 8(b)), respectively. This suggests that the lamination of organic active layers of OPV cells and OLEDs can be improved in the case where the active layers are deposited on PEDOT:PSS-coated substrates. Since the adhesion forces between the active layers and the substrates are more than the adhesion forces between stamps and the active layers, the stamps can be removed easily from the laminated active layers, without

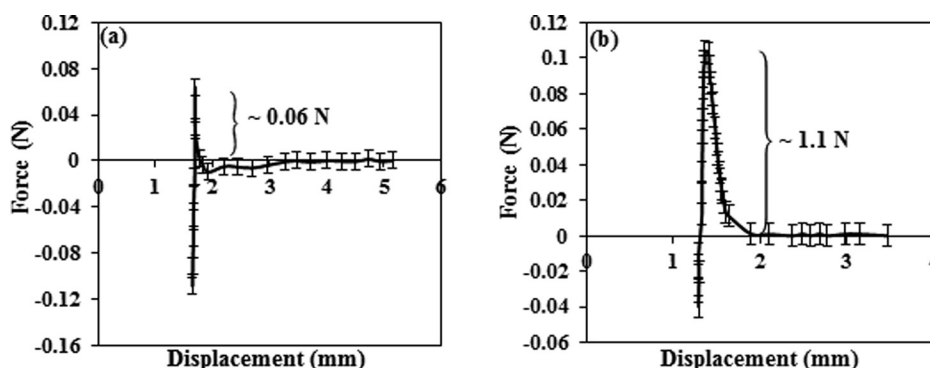


FIG. 8. Force-displacement curves of pre-lamination of (a) P3HT:PCBM and (b) MEH-PPV on PEDOT:PSS-coated glass. The peaks represent the interfacial adhesion forces along PDMS/MEH-PPV and PDMS/P3HT:PCBM interfaces during lift-off of the stamp from P3HT:PCBM and MEH-PPV.

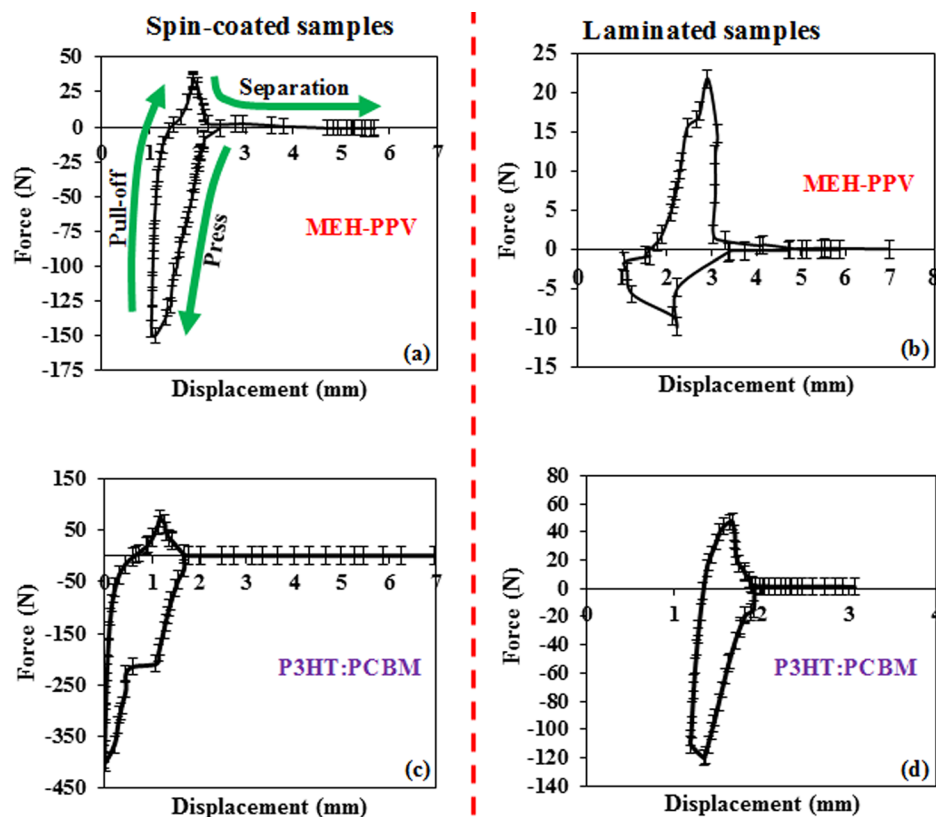


FIG. 9. Force-displacement curves of pull-off of (a) spin-coated MEH-PPV, (b) spin-coated P3HT:PCBM, (c) laminated MEH-PPV, and (d) laminated P3HT:PCBM.

damaging the interfaces between the active layers and PEDOT:PSS-coated glass.

Typical AFM images of the substrates (after the pull-off of MEH-PPV and P3HT:PCBM) are presented in Figure 10. In the case of successful lamination, no remnant of the pulled-off MEH-PPV and P3HT:PCBM was observed on the substrates after pull-off (Figures 10(a) and 10(b)). The patches of the laminated MEH-PPV and P3HT:PCBM layers are evident in the case where the layers are not fully pulled off from the substrate (Figures 10(c) and 10(d)).

D. Interfacial fracture during lift-off

It is crucial to understand the fracture along the interfaces that are involved in the lift-off stage of the lamination process. For successful lamination of any layer onto a substrate, the stamp must be lifted up successfully, without damaging the interface of interest (laminated active layers/substrates). The different categories of the possible laminations that can be achieved, based on the properties of the interfaces, have been described previously in Sec. II B.

First, the bottom interface was maintained intact, with zero edge crack length. This was done to calculate the interfacial energy release rate as a function of edge crack length at the top interface. This was done for both the lamination of P3HT:PCBM and MEH:PPV onto PEDOT:PSS-coated glass substrates. The interfacial energy release rates of the crack tips at the bottom interfaces (P3HT:PCBM/PEDOT:PSS-coated glass and MEH:PPV/PEDOT:PSS-coated glass) were also calculated for different lengths of the bottom edge cracks, keeping the top (stamp/P3HT:PCBM and stamp/MEH:PPV) edge crack length at zero. In both cases, the top

and bottom energy release rates increased with increasing crack length.

The differences between the energy release rates at the top and bottom interfaces can be observed clearly at short crack lengths (Figure 11). However, at longer crack lengths, there were no significant differences between the energy release rates of the top and bottom interfaces. Similar results have been reported by Tucker *et al.*⁷ The significant difference in the energy release rates at short crack lengths is attributed to the fact that the cracks propagate along the top and bottom interfaces, as the stamp is lifted off from the laminated layer. As such, the PDMS stamp absorbs the deformation due to lift-off.

The delamination of the stamp from the laminated layer, and the laminated layer from the substrate, during the lift-off process, becomes more interesting at the micron-scale, considering the voids that are produced as a result of the wrapping of the thin films around the nano- and micro-particles that are trapped between the substrates and laminated layers. Figure 12 presents the results of the interfacial fracture that occurs during the lift-off process.

For the lamination of both P3HT:PCBM and MEH:PPV layers, the initial energy release rate at the top interface was the maximum value. This decreased to zero, while the energy release rate at the bottom interface (that was initially at zero) increased, as the energy release rate at the top interface decreased. Meanwhile, the energy release rates of the top and bottom cracks decreased, as the length of the crack (void) created by particle increased.

Furthermore, Figure 12 shows the energy release rates (G_{void}) at the tips of the cracks, which were created by the trapped particles, increased with increasing size of the

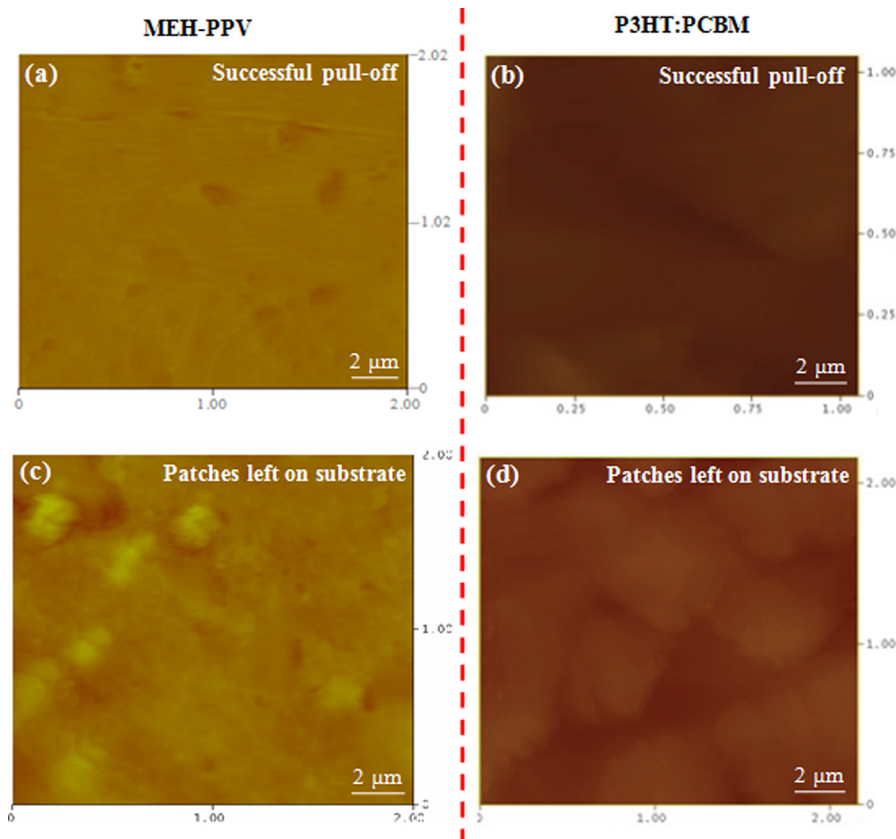


FIG. 10. Samples of the AFM images of substrates after pull-off of active layers, MEH-PPV, and P3HT:PCBM for (a) and (b) successful pull-off, (c) and (d) pull-off with remnants left on the substrates.

particle and the length of the bottom interface edge crack. However, G_{void} is very small for small particle size even as the bottom crack length increases. This is an indication that the particles can weaken the adhesion of the interface of interest during lamination. It is, therefore, important to ensure surface cleaning using laser or ozone/UV surface cleaner prior to lamination, for improving interfacial contact and adhesion between the active layer and the substrate.

The success of lamination of the active layers, P3HT:PCBM and MEH:PPV, of the electronics can be predicted in

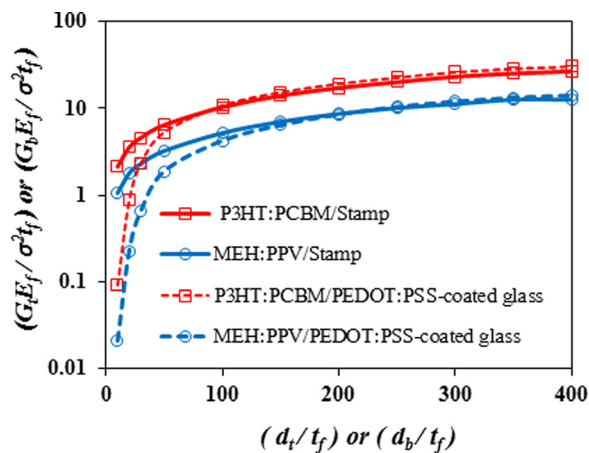


FIG. 11. The normalized top/bottom energy release rate as a function of the normalized top/bottom crack length, respectively. The energy release rates of the edge cracks at the top interfaces (P3HT:PCBM/Stamp and MEH:PPV/Stamp) were calculated with no edge crack at bottom interfaces (P3HT:PCBM/PEDOT:PSS-coated glass and MEH:PPV/PEDOT:PSS-coated glass). The energy release rates of the edge cracks at the bottom interfaces were also calculated with no edge crack at the top interfaces.

form of the differential of the interfacial energy release rates of the edge cracks at the top and bottom interfaces. This is shown in Figures 13(a) and 13(b), in which computed energy release rates are presented as a function of the normalized bottom crack length. In both cases (of the active layers), the differential energy release rates decrease with increasing normalized bottom crack length, while the increasing particle size increases the energy difference. For a critical measured value of the interfacial energy difference, we can predict the success of the lamination (as described in Sec. II C).

It is of interest to compare the computed crack driving forces with the adhesion energies^{13,18–20} and interfacial fracture energies²¹ reported previously for interfaces that are relevant to OLEDs and OPVs. These are summarized in Table II. The results obtained from the computations are comparable to the previously reported results. In the case of the OLED, in which P3HT:PCBM film is laminated onto PEDOT:PSS-coated substrates using PDMS stamp, the measured interfacial energy along the bottom interface (PEDOT:PSS/MEH-PPV) is greater than the energy along the top interface (MEH-PPV/Stamp). The small value of the interfacial energy at the top interface is attributed to the hydrophobic nature of the PDMS stamp, which facilitates successful lamination. The tendency of the crack paths to remain at the interface, or deviate away from the interface, can influence the magnitude of the computed interfacial energy, as well as the measured interfacial adhesion and fracture energies.

Similarly, in the case of OPV, the interfacial energy at the bottom interface (PEDOT:PSS/P3HT:PCBM) is more than the energy at the top interface (P3HT:PCBM/Stamp).

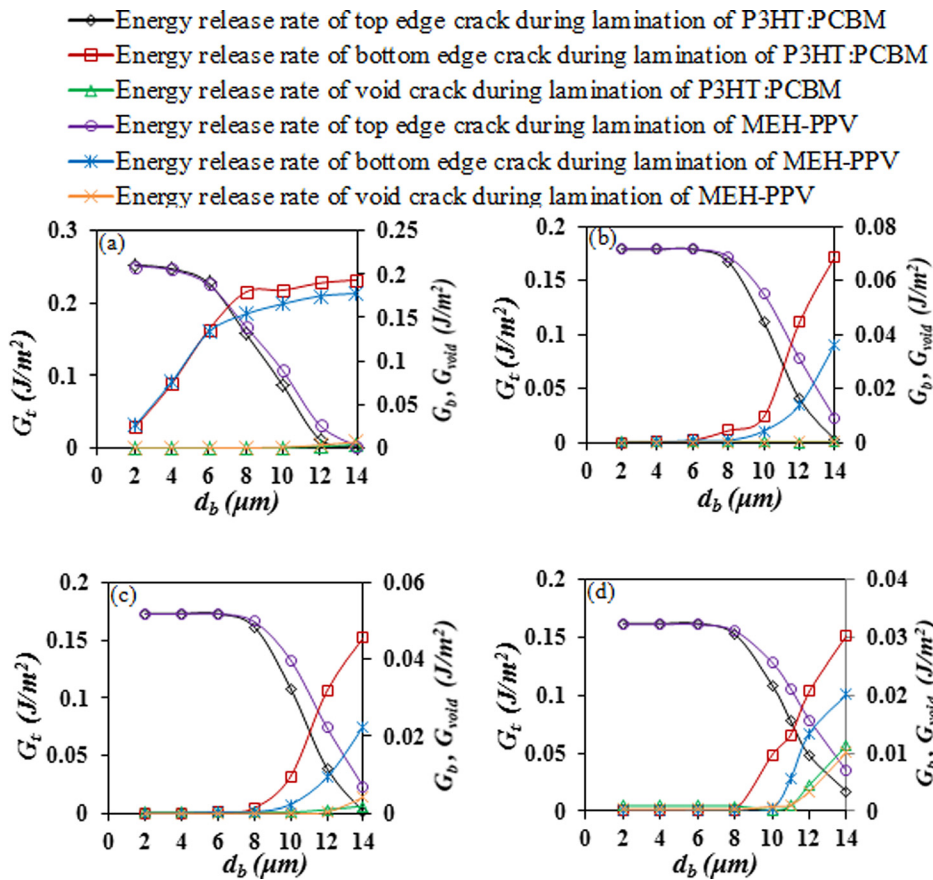


FIG. 12. Interfacial fracture during lift-up of stamp from laminated P3HT:PCBM and MEH:PPV on PEDOT:PSS-coated substrates for different particle diameters. (a) $2 \mu\text{m}$, (b) $6 \mu\text{m}$, (c) $9 \mu\text{m}$, and (d) $12 \mu\text{m}$. The concomitant energy release rates of the tips of the edge cracks at the top and bottom interfaces as functions of bottom crack length. Here, the length of the top edge crack is $6 \mu\text{m}$, while the thickness of the active layers is maintained at 200 nm .

The crack paths being remained or deviated at the interface can also be attributed to the variation in the magnitude of the computed energies, the measured interfacial adhesion, and fracture energies. Hence, interfacial fracture should occur when the interfacial fracture toughness values and the adhesion energies are lower than the substrate critical energy release rates. However, the criteria for interfacial cracking versus substrate cracking also depend on mode mixity, as shown in the earlier work by Evans *et al.*²²⁻²⁴ and Rahbar *et al.*²⁵

Finally, it should be noted that interfacial cracks can kink in-and-out of interfaces, giving rise to patches of partial interfacial separation during material pull-off. This can occur

when the mechanisms of micro-void nucleation around inclusions and interfacial impurities link with dominant interfacial cracks in ways that promote the extension of interfacial cracks into adjacent layers. In such cases, the crack can kink in-and-out of interfaces depending on the distribution of the inclusion/impurities that include the formation of voids that link up with the propagating cracks. This has been shown in earlier work by Rahbar *et al.*²⁵ using a combination of finite element simulations and experiments.

The kinking of cracks (in-and-out of interfaces) has also been discussed in prior work by Evans *et al.*^{22,24} Their work suggests that the criteria for interfacial cracking depend on the crack driving forces, as well as on the mode mixity.

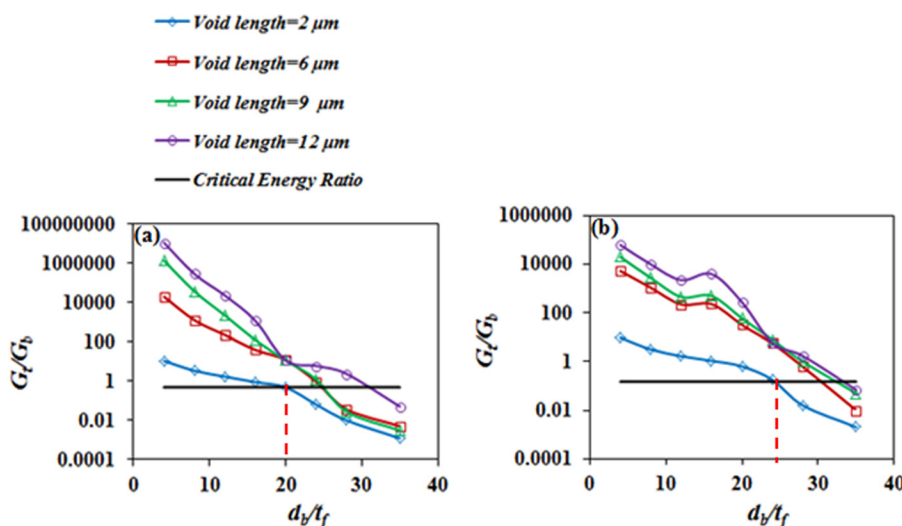


FIG. 13. Ratio of the interfacial energy release rates G_t/G_b as a function of the normalized bottom crack length (d_b/t_f), showing the influence of the particle size for (a) lamination of P3HT:PCBM, (b) lamination of MEH:PPV. Here, the thickness of the active layer is 200 nm .

TABLE II. Interfacial adhesion and fracture energies in OLEDs and OPV cells.

(a) Measured and computed interfacial energies			
Interface	Measured adhesion energy (γ) (J/m ²)	Measured fracture energy (J/m ²)	Computed energy (G) (J/m ²)
P3HT:PCBM/PEDOT:PSS (bottom)	2.6 (Ref. 20)	1.6 (Ref. 21)	1.57 (in this study)
MEH-PPV/PEDOT:PSS (bottom)	15 (Refs. 13 and 18)	...	2.42 (in this study)
P3HT:PCBM/PDMS (top)	0.75 (in this study)
MEH-PPV/PDMS (top)	0.028 (Ref. 19)	...	0.36 (in this study)
(b) Interfacial energy ratios			
Laminated layer	Computed G_{top}/G_{bottom}		
P3HT:PCBM	0.478		
MEH-PPV	0.149		

However, it did not consider the nano-scale mechanisms of microvoid nucleation and growth, as observed in the experiments and models of Rahbar *et al.*²⁴ Further work is clearly needed to include the effects of inclusion distributions microstructure-based models for the prediction of interfacial/substrate cracking and the kinking of cracks during layer pull-off processes.

E. Implications

The results presented above are significant for the fabrication of cheap organic solar cells and organic light emitting devices. They can be used as guidelines for the design of fabrication of stamps and lamination conditions that can help to improve surface contact and device performance. Furthermore, in multilayered OLEDs and OPV cells, the alignments of the layer work functions are very important in the design of improved charge transport between layers. Lamination is, therefore, a good candidate for improving contact in the multilayered structures of OLEDs and OPV cells. The application of pressure (during lamination) also tends to improve interfacial contact. However, too much pressure may cause excessive sink in and device damage. Finally, the results above provide guidelines for successful lamination of thin film structures for OLEDs and OPV cells. These guidelines are summarized in Table III.

V. CONCLUSIONS

This paper presents the results of a combined experimental and theoretical/computational study of the contact and interfacial fracture associated with the lamination of organic electronic structures.

TABLE III. Summary of the guidelines for successful lamination of thin film structures of OLEDs and OPV cells.

Void length (μm)	P3HT:PCBM	MEH-PPV	Result of lamination
2.0	$d_b/t_f \geq 20.0$	$d_b/t_f \geq 25.0$	Successful (unsuccessful otherwise)
5.0	$d_b/t_f \geq 24.5$	$d_b/t_f \geq 31.0$	Successful (unsuccessful otherwise)
9.0	$d_b/t_f \geq 25.0$	$d_b/t_f \geq 33.0$	Successful (unsuccessful otherwise)
12.0	$d_b/t_f \geq 32.0$	$d_b/t_f \geq 34.0$	Successful (unsuccessful otherwise)

1. A combination of analytical and computational models is used to study the effects of pressure on the contacts around dust particles that are trapped between adjacent layers in model OLED and OPV structures. The studies show that the contact length ratios increase with increasing pressure. However, the application of pressure may also result in excessive “sink-in” of trapped particles, which may damage the devices.
2. The subsequent pull-off stage of lamination was considered as an interfacial fracture process. This was studied using computational models of interfacial crack driving forces. The models suggest that the onset of interfacial crack growth or fracture occurred when the crack driving forces were equal to the measured adhesion energies for the relevant interfaces.
3. The effects of pre-existing defects need to be considered in greater detail, if we are to predict the critical conditions for the kinking in-and-out of cracks from different interfaces. Such kinking in-and-out is thought to contribute to the partial interfacial separation that is observed during the pull-off stage of the lamination of selected OPV and OLED structures.

ACKNOWLEDGMENTS

The research was supported by the National Science Foundation (DMR 0231418), the Princeton University Grand Challenges Program, the African Development Bank, the World Bank STEP B Program, the World Bank African Centers of Excellence Program, and the Nelson Mandela Institution. The authors also thank Professor Barry Royce for useful technical discussions.

APPENDIX A: ANALYTICAL CALCULATION OF CONTACT LENGTH AS A FUNCTION OF COMPRESSIVE FORCE

Let us consider a scenario whereby a particle is at the surface of a substrate. Any film deposited on the substrate bends round the particle like a cantilever beam with a bending energy. This is given by²⁶

$$U_b = \frac{6E_f I h^2}{S^3}, \quad (\text{A1})$$

where E_f is the film Young's modulus, I is the second moment of inertial, h is the height of the particle, and S is the length of the void created by the particle.

For a rectangular geometry, the contact surface area is given by

$$A_c = L_c \times w, \quad (\text{A2})$$

where L_c is the contact length and w is the width of the structure. The uniform pressure, P , which is applied to a cross-section area, $A_f = L \times w$, of the film can be related to the corresponding compressive force, F . This is given by

$$P = \frac{F}{Lw}, \quad (\text{A3})$$

where L is the length of the structure.

Hence, the surface energy between the film and the substrate can be written as the product of the pressure, the contact area, and the height of the particle. This is given by

$$U_s = -\frac{F}{Lw} \times (L_c \times w) \times h = -\frac{FL_ch}{L_c}. \quad (\text{A4})$$

By substituting $L_c = L - S$ into Eq. (A4), the surface energy becomes

$$U_s = -Fh \left(1 - \frac{S}{L}\right). \quad (\text{A5})$$

The total energy, U_T , is the addition of Eqs. (A1) and (A5). This is given by

$$U_T = \frac{6E_f I h^2}{S^3} - Fh \left(1 - \frac{S}{L}\right). \quad (\text{A6})$$

The length of the void can be calculated from Eq. (A6) at equilibrium, $dU_T/dS = 0$. This is given by

$$S = \left(\frac{18E_f I h L}{F}\right)^{\frac{1}{4}}. \quad (\text{A7})$$

By substituting the second moment of inertial, $I = wt_f^3/12$, into Eq. (A7), the length of the void becomes

$$S = L - L_c = \left(\frac{3E_f t_f^3 h L w}{2F}\right)^{\frac{1}{4}}. \quad (\text{A8})$$

From Eq. (A8), we write the contact length as a function of the compressive force. This is given by

$$\frac{L_c}{L} = 1 - \left(\frac{3E_f t_f^3 h w}{2FL^3}\right)^{\frac{1}{4}}. \quad (\text{A9})$$

APPENDIX B: INTERFACIAL ENERGY RELEASE RATE

$$G = f(\bar{E}_s, \bar{E}_f, t_f, t_s, d_b, d_t, \sigma)$$

Number of parameters = 8

Number of fundamental dimension = 3

Number of dimensionless quantities = 8 - 3 = 5

The core variables are

$$\sigma = [ML^{-1}T^{-2}], \quad \bar{E}_f = [ML^{-1}T^{-2}], \quad \text{and } t_f = [L].$$

$$\sigma^2 t_f^2 = [M^2 L^{-2} T^{-4}] [L^2] = [M^2 T^{-4}], \quad (\text{B1})$$

$$\bar{E}_f t_f = [ML^{-1}T^{-2}] [L] = [MT^{-2}]. \quad (\text{B2})$$

By dividing Eq. (B1) by (B2)

$$\frac{\sigma^2 t_f^2}{\bar{E}_f t_f} = \frac{\sigma^2 t_f}{\bar{E}_f} = \frac{[M^2 T^{-4}]}{[MT^{-2}]} = [MT^{-2}]. \quad (\text{B3})$$

First dimensionless quantity (π_1):

$$G = [MT^{-2}] = \frac{\sigma^2 t_f}{\bar{E}_f},$$

$$\pi_1 = \frac{G \bar{E}_f}{\sigma^2 t_f}.$$

Second dimensionless quantity (π_2):

$$\bar{E}_f = [ML^{-1}T^{-2}],$$

$$\pi_2 = \bar{E}_s [LT^2 M^{-1}] = \frac{\bar{E}_s}{\bar{E}_f}.$$

Third dimensionless quantity (π_3):

$$t_s = [L],$$

$$\pi_3 = t_s [L^{-1}] = \frac{t_s}{t_f}.$$

Fourth dimensional quantity (π_4):

$$d_b = [L],$$

$$\pi_4 = d_b [L^{-1}] = \frac{d_b}{t_f}.$$

Fifth dimensional quantity (π_5):

$$d_t = [L],$$

$$\pi_5 = d_t [L^{-1}] = \frac{d_t}{t_f},$$

$$\pi_1 = f(\pi_2, \pi_3, \pi_4, \pi_5),$$

$$\frac{G \bar{E}_f}{\sigma^2 t_f} = f\left(\frac{\bar{E}_s}{\bar{E}_f}, \frac{t_s}{t_f}, \frac{d_b}{t_f}, \frac{d_t}{t_f}\right),$$

$$G = f\left(\frac{\bar{E}_s}{\bar{E}_f}, \frac{t_s}{t_f}, \frac{d_b}{t_f}, \frac{d_t}{t_f}\right) \frac{\sigma^2 t_f}{\bar{E}_f}. \quad (\text{B4})$$

¹J.-Y. Lee, S. T. Connor, Y. Cui, and P. Peumans, *Nano Lett.* **10**, 1276 (2010).

²J. Huang, G. Li, and Y. Yang, *Adv. Mater.* **20**, 415 (2008).

³T.-F. Guo, S. Pyo, S.-C. Chang, and Y. Yang, *Adv. Funct. Mater.* **11**, 339 (2001).

⁴T. Zyung, S. H. Kim, S.-C. Lim, J. H. Lee, H. Y. Chu, and J.-K. Oh, *J. Korean Phys. Soc.* **48**, S111 (2005).

⁵S. R. Forrest, *Nature* **428**, 911 (2004).

- ⁶W. O. Akande, Y. Cao, N. Yao, and W. Soboyejo, *J. Appl. Phys.* **107**, 043519 (2010).
- ⁷M. B. Tucker, D. R. Hines, and T. Li, *J. Appl. Phys.* **106**, 103504 (2009).
- ⁸Y. Cao, C. Kim, S.-R. Forrest, and W. Soboyejo, *J. Appl. Phys.* **98**, 033713 (2005).
- ⁹Y.-R. Jeng, M.-L. Guo, H.-C. Li, and T.-F. Guo, *Electrochem. Solid-State Lett.* **10**, D139 (2007).
- ¹⁰J. Du, T. Tong, W. Akande, A. Tsakiridou, and W. Soboyejo, *J. Disp. Technol.* **9**, 601 (2013).
- ¹¹L. Hu, H. Wu, F. Lamantia, Y. Yang, and Y. Cui, *ACS Nano* **4**, 5843 (2010).
- ¹²C. Kim, Y. Cao, W. O. Soboyejo, and S. R. Forrest, *J. Appl. Phys.* **97**, 113512 (2005).
- ¹³D. Yu, O. K. Oyewole, D. Kwabi, T. Tong, V. C. Anye, J. Asare, E. Rwenyagila, A. Fashina, O. Akogwu, J. Du, and W. O. Soboyejo, *J. Appl. Phys.* **116**, 074506 (2014).
- ¹⁴D. Tahk, H. H. Lee, and D.-Y. Khang, *Macromolecules* **42**, 7079 (2009).
- ¹⁵W. Soboyejo, *Mechanical Properties of Engineered Materials* (CRC, New York, 2003).
- ¹⁶A. Bietsch and B. Michel, *J. Appl. Phys.* **88**, 4310 (2000).
- ¹⁷N. Bowden, S. Brittain, A. G. Evans, J. W. Hutchinson, and G. M. Whitesides, *Nature* **393**, 146 (1998).
- ¹⁸T. Tong, B. Babatope, S. Admassie, J. Meng, O. Akwogu, W. Akande, and W. O. Soboyejo, "Adhesion in organic electronic structures," *J. Appl. Phys.* **106**, 083708 (2009).
- ¹⁹S.-H. Hur, D.-Y. Khang, C. Kocabas, and J. A. Rogers, *Appl. Phys. Lett.* **85**, 5730 (2004).
- ²⁰T. Michelle Tong, "Adhesion and interfacial fracture: From organic light emitting devices and photovoltaic cells to solar lanterns for developing regions," Ph.D. thesis (Princeton University, 2012).
- ²¹S. R. Dupont, M. Oliver, F. C. Krebs, and R. H. Dauskardt, *Sol. Energy Sol. Cells* **97**, 171 (2012).
- ²²A. G. Evans and J. W. Hutchinson, *Acta Metall. Mater.* **37**, 909 (1989).
- ²³M. Y. He, H. Cao, and A. G. Evans, *Acta Metall. Mater.* **38**, 839 (1990).
- ²⁴A. G. Evans, B. J. Dalgleish, M. He, and J. W. Hutchinson, *Acta Metall.* **37**, 3249 (1989).
- ²⁵N. Rahbar, Y. Yang, and W. O. Soboyejo, *Mater. Sci. Eng., A* **488**, 381 (2008).
- ²⁶Y. Zhang and Y.-P. Zhao, *Sens. Actuators, A* **171**, 381 (2011).